Multiple strategies to decrease ignition temperature for soot combustion on ultrathin MnO_{2-x} nanosheet array

Qiaolan Shi[a], Taizheng Liu[a], Qian Li[a], Ying Xin[a], Xingxu Lu[b], Wenxiang Tang[b], Zhaoliang Zhang[a,*], Pu-Xian Gao[b,*], James A. Anderson[c,*]

[a] School of Chemistry and Chemical Engineering, Shandong Provincial Key Laboratory of Fluorine Chemistry and Chemical Materials, University of Jinan, No. 336, West Road of Nan Xinzhuang, Jinan, 250022, China
[b] Nanomaterials Science Laboratory, Department of Materials Science and Engineering & Institute of Materials Science, University of Connecticut, 97 N. Eagleville Rd., Storrs, CT, 06269-3136, USA
[c] Surface Chemistry and Catalysis Group, Materials and Chemical Engineering, University of Aberdeen, AB24 3UE, United Kingdom

ABSTRACT

Diesel soot combustion suffers from ignition temperatures (T_{10}) as high as > 450 °C in the absence of catalysts, which are unavailable in diesel exhaust during normal driving cycles (normally 200–400 °C). A catalytic diesel particulate filter (CDPF) could decrease T_{10} greatly, but it is often inadequate due to the poor contact associated with the solid (catalyst)-solid (soot) interactions. Herein, a highly significant T_{10}, as low as ~200 °C, was achieved on noble metal-free ultrathin MnO_{2-x} nanosheet array fabricated by *in situ* etching of a La layer from $LaMnO_3$ under loose contact conditions in a NO-containing atmosphere. A number of advantages were found with such a system including the improved reducibility. Then, the nanosheet array ensures high dispersion of soot on the catalyst. Finally, high NO-to-NO_2 oxidation activity further facilitates contact between catalyst and soot via NO_2, a stronger oxidant than O_2.

1. Introduction

Soot particulates with the elemental carbon core are among the most toxic components emitted by diesel engines. However, typical diesel engine exhaust temperatures during normal driving cycles fall within the 200–400 °C range, which leads to research and development of oxidation/combustion catalysts coated on diesel particulate filters (CDPF) to decrease soot ignition temperature T_{10} (at which soot conversion reaches 10%) from non-catalytic > 450 to 200 °C [1,2]. The low T_{10} also avoids thermal degradation of the downstream ammonia selective catalytic reduction (SCR) catalysts of NO_x [3]. Unfortunately, this goal is far from being achieved [4,5]. The T_{10} was decreased to 214 °C under loose contact conditions between catalyst and soot in a 2000 ppm NO + 5% O_2 atmosphere by using noble-metal Au@Pt core-shell nanoparticles supported on three-dimensionally ordered macroporous (3DOM) Ce-Zr oxides [6,7], representing great progress. Recently, Davies et al reported that soot can be initiated catalytically at 200 °C by *in-situ* generated N_2O from coupled non-selective NO_x reduction with NH_3 on 2 wt.% $Ag/Ce_{0.35}Zr_{0.15}Al_{0.5}O_{1.75}$ [8].

Soot combustion is a solid (reactant)-solid (catalyst)-gas (oxidant) system. Consequently, the contact between soot and catalyst plays a

pivotal role in determining T_{10}. Generally, three strategies have been followed till now. One is intrinsic, namely, improvement of the redox property of catalysts in order to produce highly oxidizing active oxygen species [7]. This is also beneficial to the second strategy, namely oxidizing soot by NO_2, a more active oxidant than O_2, which is formed via catalytic oxidation of effluent NO over diesel oxidation catalysts (DOC), namely, the so-called Continuously Regenerating Traps (CRT) developed by Johnson Matthey [9]. Generally, expensive noble metals (such as Pt) are common components of oxidation catalysts. However, the undesirable ultra-low quantities of Pt would migrate from the upstream DOCs/CDPF to SCR catalysts, leading to poor NO_x conversion via catalytic NH_3 oxidation into NO_x and N_2O [10]. Actually, it has been shown that the performance can be prevented by the ppm contaminants of Pt on the SCR catalysts [11]. Transition metal oxides are intriguing alternatives for NO oxidation. MnO_x-based oxides are strong oxidants [12] and have the potential to substitute current commercial Pt-based catalysts [13–16]. The third strategy is changing catalyst morphology from particles [12] to nanobelts [17], nanosheets [18,19], nanowires [20], nanotubes [21], mesoporous [22] and macroporous [23,24] structures in order to increase the dispersion of soot particles on the catalysts. However, ultrathin MnO_{2-x} nanosheet array, which possess a

---

more accessible surface configuration and more exposed surface atoms that can facilitate high dispersion of soot particles and contact with active sites, and more significantly, combine all three strategies, have not been reported to date.

Mn oxides show many environmental applications [25], such as catalytic CO oxidation [26], volatile organic compound (VOC) combustion [27], and ammonia SCR of NO_x [28]. In this work, through *in situ* etching a La layer from $LaMnO_3$ (LMO) perovskite, first proposed by the group of Li [29–31], ultrathin MnO_{2-x} nanosheet arrays on $LaMnO_3$ substrates were fabricated, which provide multi-advantages for soot combustion: high soot dispersion on nanosheets, improved redox property, and high NO-to-NO_2 oxidation activity. As a result, a T_{10}, as low as ~200 °C, under loose contact conditions between soot and catalyst without noble metals in the NO-containing atmosphere, was achieved.

2. Experimental

2.1. Synthesis of LaMnO₃

4.3291 g $La(NO_3)_3 \cdot 6H_2O$ and 3.5790 g $Mn(NO_3)_2$ (50 wt%) were dissolved in deionized water at room temperature under stirring for several minutes. 6.3042 g $C_6H_8O_7 \cdot H_2O$ was added into the above solution with stirring until a clear solution was obtained. The resulting solution was heated at 80 °C and evaporated to dryness with vigorous stirring. The sample was further dried overnight in an oven at 80 °C. Then the sample was calcined at 350 and 750 °C for 2 and 4 h, respectively in static air. The heating rate was 5 °C/min. The material obtained was $LaMnO_3$.

2.2. Selective etching of La from LaMnO₃

0.2500 g $LaMnO_3$ powder was added to 25 ml HNO_3 solution (3 mol/L) and the mixture was stirred at room temperature for either 4–6 or 7 h. After filtration, the resultant solid was washed with deionized water until a pH of 7 was attained and then dried overnight at 80 °C. The as-prepared samples were denoted as LMO-*n*, where *n* represents etching times, 4–7.

2.3. Synthesis of γ-MnO₂ as a control sample

γ-MnO_2 was synthesized by a redox reaction process [32]. 7.9017 g $KMnO_4$ and 29.6865 g $MnCl_2$ were dissolved in 100 mL of deionized water. Subsequently, the $KMnO_4$ solution was dropped slowly into the $MnCl_2$ solution under stirring at room temperature. The precipitates were filtered, washed with deionized water, and then dried at 100 °C for 12 h before annealing for 24 h at 200 °C.

2.4. Characterizations

X-ray powder diffraction (XRD) patterns were measured on a D8 FOCUS powder X-ray diffraction instrument (Bruker AXS, Germany) using 40 kV as tube voltage and 40 mA as tube current.

Surface area and pore size distribution were determined by N_2 adsorption/desorption at 77 K using Brunauer-Emmett-Teller (BET) method with a Micromeritics ASAP 2020 instrument after out-gassing for 5 h at 300 °C prior to analysis.

Field-emission scanning electron microscopy (FESEM) equipped with energy dispersive spectroscopy (EDS) was performed on a Hitachi SU-70 microscope.

High-angle annular dark-field (HAADF) images were obtained on an FEI Talos S/TEM (Scanning/Transmission Electron Microscope).

X-ray photoelectron spectroscopy (XPS) data were obtained on a Thermo Scientific ESCALAB 250XI electron spectrometer, using monochromatic Al Kα as the exciting radiation at a constant pass energy of 1486.6 eV. The binding energies (BE) values were calibrated
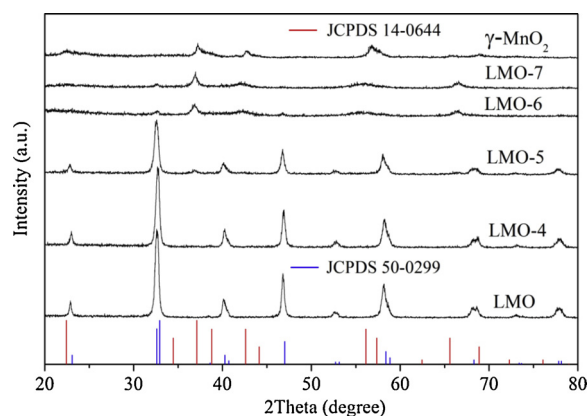

Fig. 1. XRD patterns for LMO, LMO-*n* and MnO_2.

with the signal of contaminated carbon C1 s at 284.8 eV. The spectra were deconvoluted using XPSPEAK software.

Temperature programmed reduction with H_2 (H_2–TPR) experiments were performed in a quartz reactor with a thermal conductivity detector (TCD) to monitor H_2 consumption. A 50 mg sample was pretreated in situ for 30 min. at 200 °C in a flow of O_2 (30 ml/min) and cooled to room temperature in the presence of O_2. After purging in N_2, TPR was conducted at 10 °C/min up to 900 °C in a 30 mL/min flow of 5 vol.% H_2 in N_2. To quantify the total amount of H_2 consumption, the CuO was used as a calibration reference. The initial hydrogen consumption rate was used to evaluate the redox performance of different catalysts, presented as hydrogen consumption per unit time of the sample per unit mole. Using the H_2-TPR data, the first 20% of the total amount of hydrogen consumed is used to calculate the initial hydrogen consumption rate of the catalyst.

NO oxidation reactions were performed in a fixed-bed quartz reactor. The catalyst (147 mg) was held in a quartz tube by packing quartz wool at both ends of the catalyst bed. The reaction mixture containing NO (500 ppm), O_2 (5%) and He was fed to the reactor at a flow rate of 100 mL/min. The effluent gas was analyzed by a NO_x analyzer (Modle-42i-HL, Germany). The activity at each temperature was obtained when the reaction was stable after more than 30 min.

In situ IR spectra were recorded using a Bruker Tensor 27 spectrometer over the range 4000-400 cm^{-1}, with 16 scans, at a resolution of 4 cm^{-1}. Self-supporting wafers were pretreated in the IR cell at 175 °C in a flow of He for 30 min to remove any adsorbed species. After the background spectrum was recorded, the IR spectra were recorded in the flow of 500 ppm NO + He (100 mL/min).

2.5. Catalytic activity

Temperature-programmed oxidation (TPO) reactions were conducted in a fixed bed micro-reactor. Printex-U from Degussa is used as the model soot. Two conditions (tight and loose contact) were employed in this study, in which 147 mg of catalyst and 3 mg of soot were used. The high weight ratio of catalyst to soot is used because advance diesel engines emit ever less soot [33,34]. In tight contact conditions, soot was mixed with the catalyst in an agate mortar for 30 min to obtain a homogeneous mixture. In loose contact conditions, the catalyst-soot mixture was added into a small flask and shaken for 24 h. 150 mg sample of the soot-catalyst mixture was pretreated in a flow of He (100 mL/min) at 200 °C for 30 min to remove adsorbed species. After cooling to room temperature, a gas flow with 5 vol.% O_2 (or 5 vol.% O_2 + 500 ppm NO) in He was introduced and then the TPO was started at a heating rate of 5 °C/min until reaching 650 °C. To compare with literature values, an identical set of conditions as employed elsewhere [6] was established, i.e. TPO under loose contact conditions with catalyst/soot = 10:1 in a gas mixture of 2000 ppm NO + 5 vol.% O_2. The
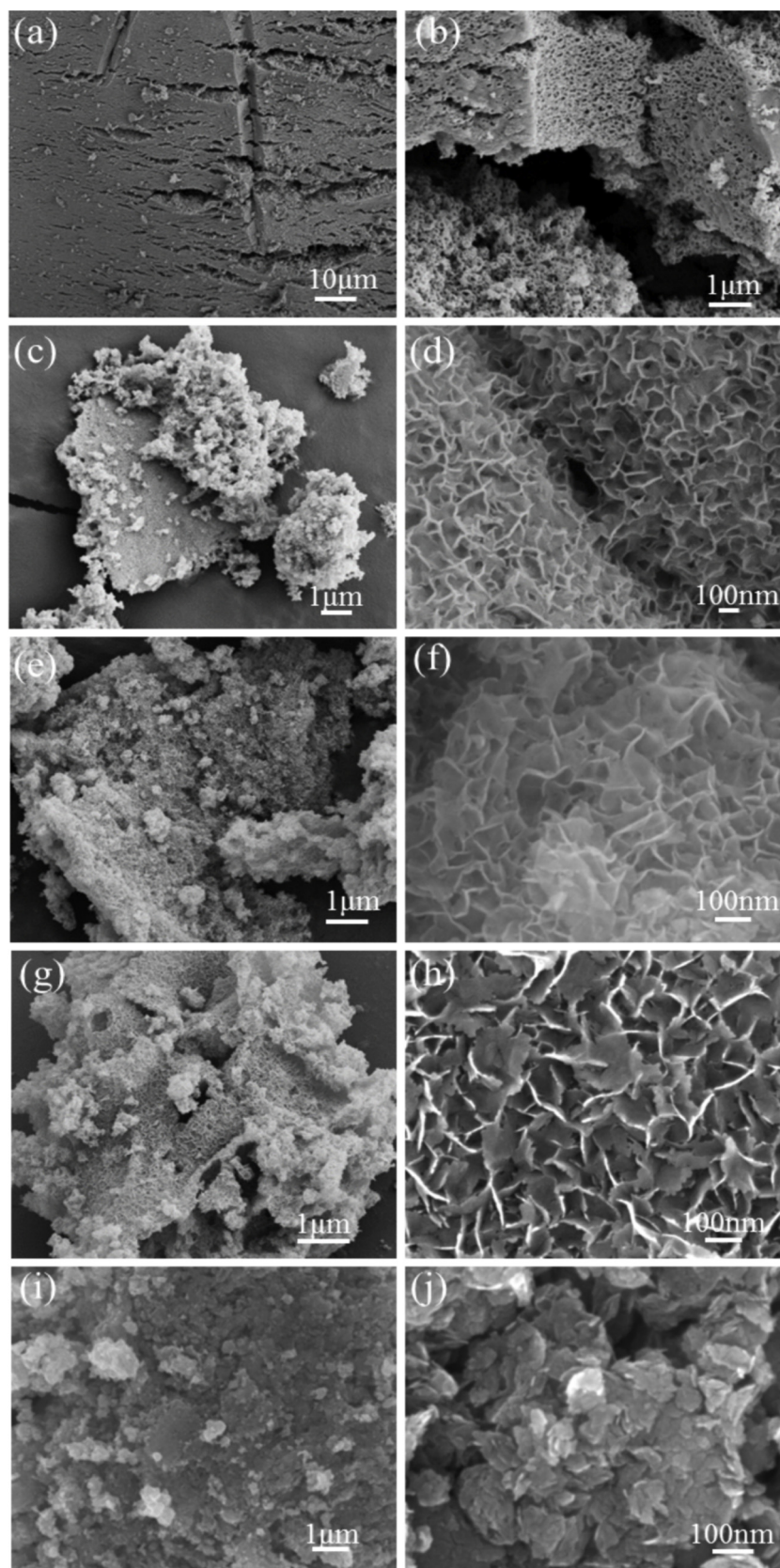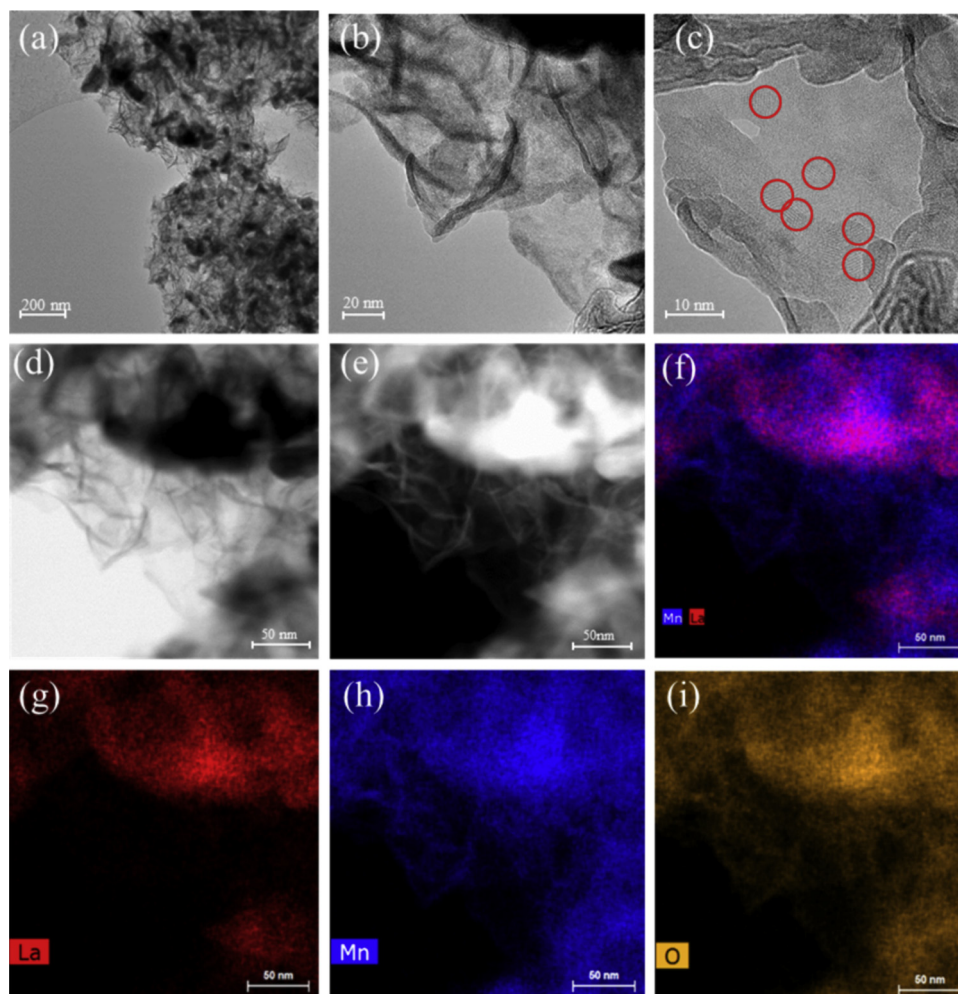
Fig. 2. SEM images for LMO (a, b), LMO-4 (c, d), LMO-5 (e, f), LMO-6 (g, h) and LMO-7 (i, j).

Table 1
Compositions, textural properties and XPS data.

Samples	La/Mn (Molar)[a]	S_{BET} (m^2 g^{-1})	V_p (cm^3 g^{-1})	Pore diameter (nm)	Mn^{4+}/Mn^{3+} (Molar)	La/Mn (Molar)[c]	O_{ads}/O_{latt} (Molar)[b]
LMO	1.075	12	0.036	11.82	0.60	1.21	0.73
LMO-4	0.667	63	0.294	12.86	1.04	0.26	0.71
LMO-5	0.292	94	0.325	13.82	1.10	0.13	0.78
LMO-6	0.031	219	0.845	15.46	1.58	0.10	0.67
LMO-7	0.002	204	0.705	13.82	1.74	0.07	0.51
MnO$_2$	–	81	0.285	14.16	1.88	–	0.21

a: from SEM; b, c and d: from XPS; b: O_{ads}/O_{latt} represents the ratio of lattice oxygen and adsorbed oxygen from XPS.

Fig. 3. TEM images (a and b), HRTEM image (c), HAADF images (d and e), the corresponding EDS elemental mapping of La + Mn (f), La (g), Mn (h), O (i) for LMO-5. Circles in (c) indicate nanoparticles of MnO$_{2-x}$.

effluent gases were monitored online using a gas chromatograph (GC, SP-6890, Shandong Lunan Ruihong Chemical Instrument Corporation, China) fitted with a methanator or a IR continuous gas analyzer (MKS MultiGas 2030, USA).

The activity for soot combustion was evaluated by the ignition temperature T_{10}, which is defined as the temperature at which 10% of the soot is converted. In comparison with subsequent combustion, reflected by T_{50} and T_{90}, the ignition of soot is the critical first step. As so as soot ignites, a sequence of consecutive oxidation steps takes place easily [8]. The selectivity to CO$_2$ (S_{CO_2}) is defined as the percentage CO$_2$ in the outlet concentration divided by the sum of the CO$_2$ and CO outlet concentrations.

The intrinsic activity, turnover frequency (TOF), is measured by an isothermal anaerobic titration with soot as a probe molecule, as suggested previously [35]. A 50 mg mixture of catalyst and soot (49:1) below 300 mesh was diluted with 100 mg silica (below 300 mesh also). After pretreatment in a flow of He (100 mL/min) at 120 °C for 30 min, a gas flow with 5 vol.% O$_2$ in He (150 mL/min) was introduced. The isothermal reaction rates were detected at 120 °C when the soot conversion is stable and low but sufficient for analysis purposes. After 30–60 min, O$_2$ was replaced with He. The transient decay in concentrations from the steady state was monitored using a quadruple mass spectrometer (MS, OmniStar 200, Balzers) with a m/z of 44 for CO$_2$ and 32 for O$_2$. The number of active redox sites available to soot under these reaction conditions can be quantified by integrating the diminishing rate of CO$_2$ formation over time.
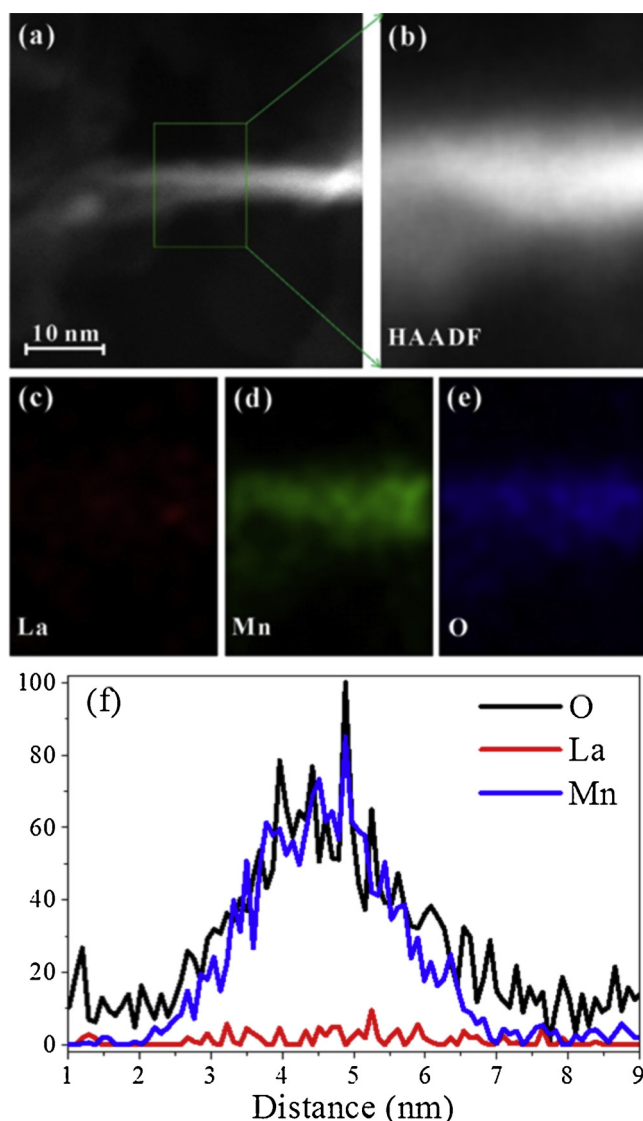
Fig. 4. HAADF images (a, b), the corresponding EDS elemental mapping of La (c), Mn (d), O (e), line scanning (f) for a single sheet MnO_{2-x} from LMO-5.

3. Results and discussion

Fig. 1 shows the XRD patterns of LMO-*n*, including LMO and γ-MnO$_2$ for references. A single-phase rhombohedral structure is observed for the original LMO sample (JCPDS 50-0299). With an etching time of 4–5 h, the intensity of the LMO peaks decreases accompanying by the appearance of a new peak at $2\theta \approx 37°$. For LMO-6 and LMO-7, the LMO phase almost disappears, while the 37° peak and others become evident, which can be ascribed to γ-MnO$_2$ (JCPDS 14-0644). However, these newly appeared peaks are very broad, suggesting the presence of a poorly crystalline phase with significant structural defects or distortion, as in the case of the control sample γ-MnO$_2$ (Fig. S1). Most likely, the γ-MnO$_{2-x}$ phase is formed in addition to the residual LMO. According to quantitative XRD analysis using the reference intensity ratio (RIR) method [35], the weight ratios of γ-MnO$_{2-x}$ to LMO are about 0.05 and 10.8 for LMO-5 and LMO-6, respectively (data for LMO-4 and LMO-7 cannot be obtained reliably due to large errors).

The morphology of LMO-*n* is first checked by SEM (Fig. 2). LMO is composed of sponge-like bulk (Fig. 2a and b). Interestingly, LMO-4 (Fig. 2c and d), LMO-5 (Fig. 2e and f) and LMO-6 (Fig. 2g and h) show the nanosheet array on the residual LMO substrate. Taking LMO-5 as an example (Fig. S2), there are about 250 nanosheets with a length and

width of 100 nm and 100 nm, respectively, within an area of 1 μm^2 visually. However, the nanosheet array is almost completely lost for LMO-7, which shows a significantly agglomerated lamellar morphology (Fig. 2i and j). EDS shows a decrease in the La/Mn ratio with the increased etching time from 4 to 7 h (Fig. S2 and Table 1), confirming the selective etching of La cations in LMO.

The nanosheet morphology is further evidenced by HAADF-STEM for LMO-5 as an example (Fig. 3a and b). The HRTEM images show that the nanosheets contain many small nanoparticles around 5 nm (Fig. 3c), suggesting polycrystallinity of the nanosheets. Elemental mapping of La, Mn and O confirmed the nanosheets are MnO$_{1.7}$ species (Fig. 2 d–i), demonstrating exfoliation of the La layers. The thickness of the nanosheets is about 3 nm (Fig. 4a and b) with only Mn and O detected by EDS mapping (Fig. 4c–e) and line scanning (Fig. 4f). The as-fabricated ultrathin MnO$_{2-x}$ sheets after losing La atoms in LMO would possess abundant dangling bonds with high reactivity [36].

Fig. 5 shows N$_2$ adsorption/desorption isotherms and pore distribution curves (inset), characteristic of a combination of mesoporous and macroporous (> 50 nm) structures. The mesopores are among nanoparticles constituting nanosheets as observed from HRTEM, while the macropores are attributed to the nanosheet array as shown in Fig.2. As expected from the nanosheet morphology, BET surface areas and pore volumes for LMO-*n* increase significantly compared with LMO and reach a maximum at LMO-6 (Table 1). The average pore diameters show a similar tendency, but are limited to the 10–20 nm range, which is less than soot particle sizes from diesel engines (> 25 nm) [37], suggesting that soot would be mainly dispersed on the surface of nanosheets.

Surface information including element compositions, valences and adsorption species are detected by XPS (Fig. 6 and Table 1). Mn2p spectra show the presence of Mn^{4+} and Mn^{3+}. In the O 1 s spectra, three types of oxygen species, lattice oxygen (O$_{latt}^{2-}$), surface chemically adsorbed oxygen (O$_{ads}$, including O$_2$-, O$_2^{2-}$ and O-), and surface carbonates/ hydroxyl are detected. Furthermore, both the peaks of Mn2p and O1 s shift from that of LMO towards that of γ-MnO$_2$, and the positions of the Mn2p and O1 s peaks for LMO-6 and LMO-7 are similar to γ-MnO$_2$, consistent with XRD results. On a quantitative basis, the Mn^{4+}/Mn^{3+} ratio increases with the etching time from 4 to 7 h, suggesting an increase in the MnO$_{2-x}$ content. This is also confirmed by quantitative analyses of the surface La/Mn ratios (Table 1). It has been reported that O$_{ads}$ has an extremely high reactivity toward soot oxidation even at a low temperature of 150 °C [38], which reaches the maximum at LMO-5 for LMO-*n* (Table 1).

The redox properties were investigated by H$_2$-TPR (Fig. 7a). A typical H$_2$-TPR profile is observed for LMO [39,40]. The low-temperature peak at about 350 °C and a shoulder involve the reduction of Mn^{4+} to Mn^{3+} and Mn^{3+} located in a coordination-unsaturated microenvironment to Mn^{2+}, respectively [39], while the wide high-temperature peak at $> \tilde{\ }700$ °C is attributed to the reduction of the remaining Mn^{3+} to Mn^{2+} [40]. However, all LMO-*n* samples show similar profiles to γ-MnO$_2$ below 500 °C with two peaks corresponding to the stepwise reduction of MnO$_2$ to Mn$_2$O$_3$, Mn$_3$O$_4$ and MnO [41], while the high-temperature peak ($> \tilde{\ }700$ °C) is attributed to bulk LMO reduction, which is not detected for LMO-7, confirming the negligible LMO content after prolonged etching times, in accordance with XRD and EDS analysis (Table 1). It is widely accepted that the low-temperature reducibility of catalysts can be evaluated by using the initial H$_2$ consumption rates, where less than 20% oxygen in the catalysts is removed for the first reduction peak [42]. As shown in Fig. 7b, the reducibility increases following the sequence LMO $< \gamma$-MnO$_2 <$ LMO-4 $<$ LMO-5 $<$ LMO-7 $<$ LMO-6, in accordance with the fact that the thin nanosheets possess more exposed active sites with lower coordination and dangling bonds due to etching of neighbouring La atoms [36]. Our previous work has confirmed that soot combustion takes place via readily reducible lattice oxygen following a Mars van Krevelen (MvK) mechanism [35,38].
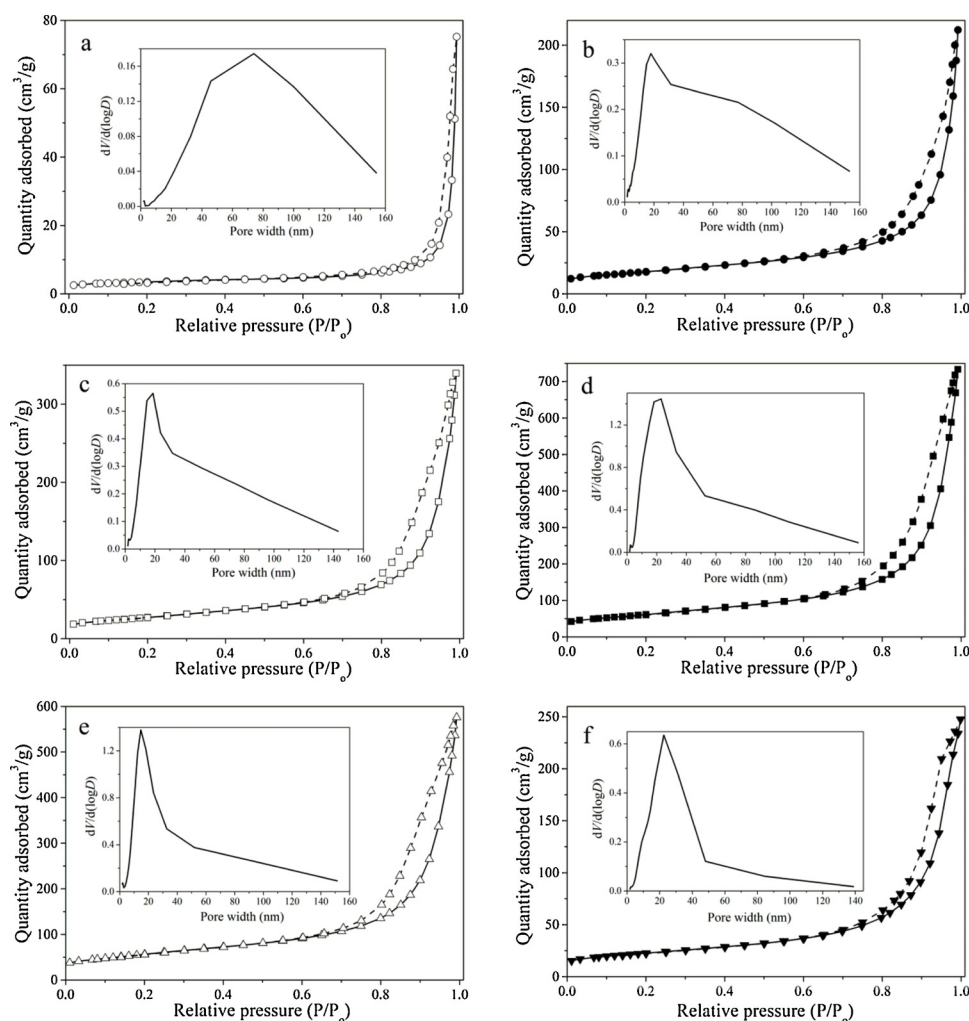
Fig. 5. N$_2$ adsorption/desorption isotherms and pore distribution (inset) curves for LMO (a), LMO-4 (b), LMO-5 (c), LMO-6 (d), and LMO-7 (e).
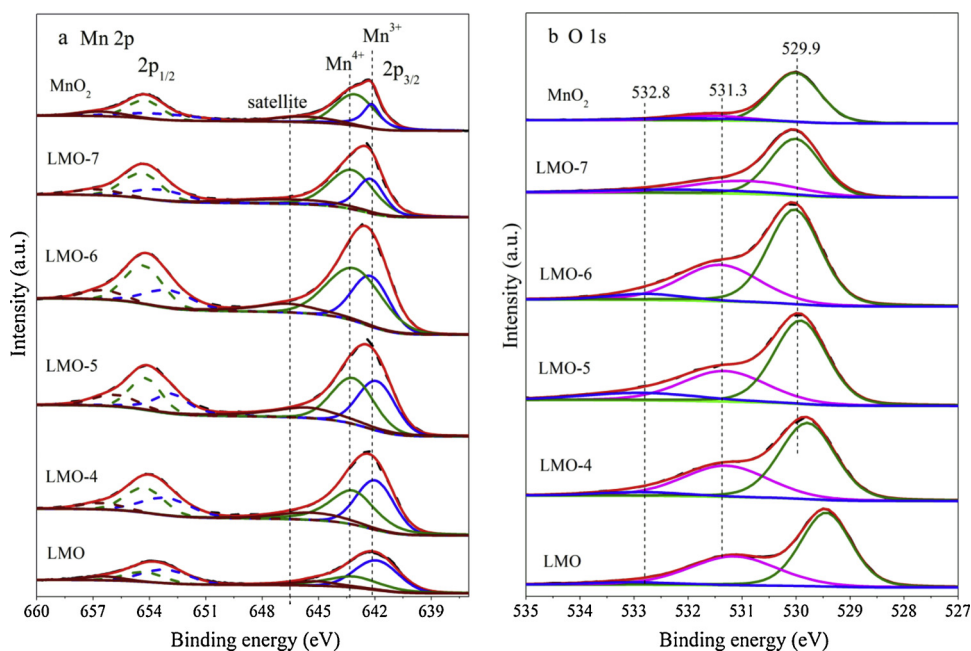

Fig. 6. Mn 2p (a) and O1s (b) XPS spectra for LMO-*n*, LMO and MnO$_2$.
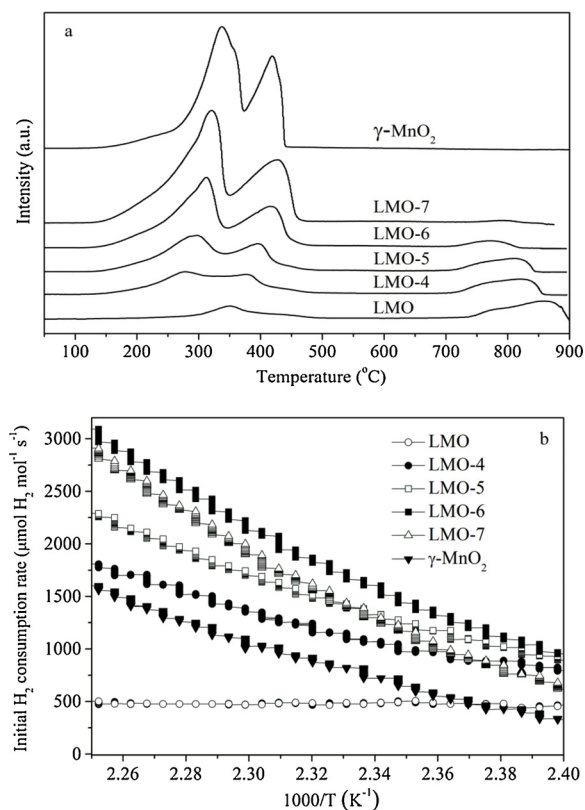
Fig. 7. H$_2$-TPR (a) and initial H$_2$ consumption rate from H$_2$-TPR (b).
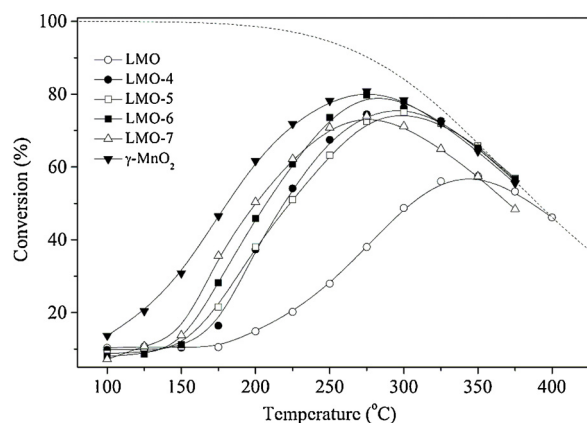

Fig. 8. NO conversion to NO$_2$ as a function of temperature in a gas mixture of 500 ppm NO + 5% O$_2$.

Table 2
Catalysts activity expressed as NO conversion at 200°C and T_{10}.

Samples	NO conversion at 200°C (%)	Loose in O$_2$ + 500 ppmNO[a]	Loose in O$_2$[b]	Tight in O$_2$[c]	Loose in O$_2$ + 2000 ppmNO[d]
LMO	15	334	400	306	342
LMO-4	37	204	369	217	309
LMO-5	38	203	377	188	202
LMO-6	46	198	342	192	279
LMO-7	50	325	363	298	304
MnO$_2$	62	323	361	324	308

a: Loose contact with catalyst/soot = 49:1 in 5 vol.% O$_2$ + 500 ppm NO; b: Loose contact with catalyst/soot = 49:1 in 5 vol.% O$_2$; c: Tight contact with catalyst/soot = 49:1 in 5 vol.% O$_2$; d: Loose contact with catalyst/soot = 10:1 in 5 vol.% O$_2$ + 2000 ppm NO (conditions identical to [6] to allow comparison).
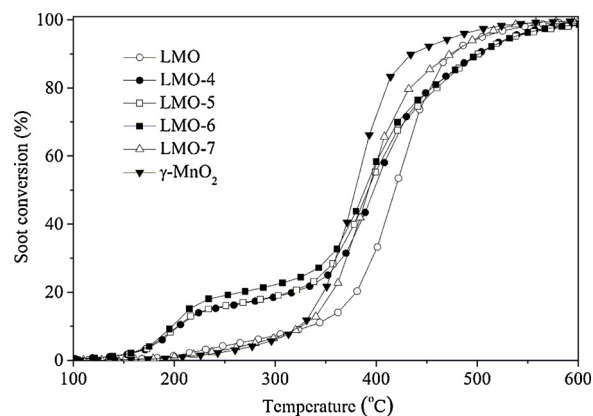

Fig. 9. Soot conversion under the loose contact condition between catalyst and soot in a gas mixture of 500 ppm NO + 5 vol.% O$_2$ in He.
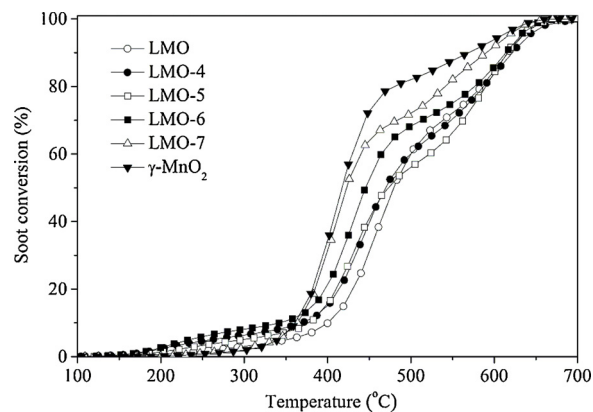

Fig. 10. Soot conversion under loose contact between catalyst and soot in 5 vol. % O$_2$ in He.
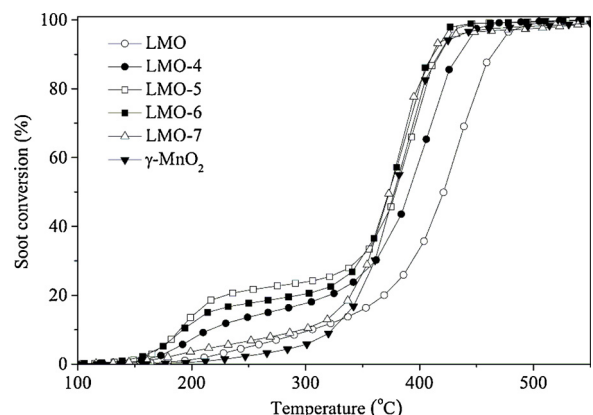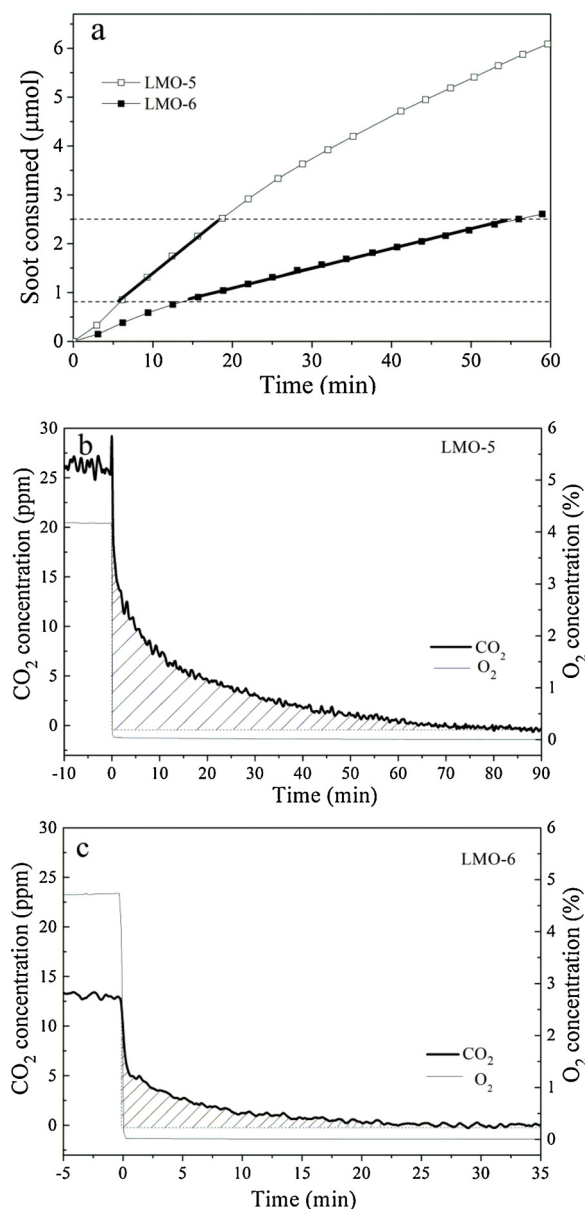

Fig. 11. Soot conversion under the tight contact between catalyst and soot in 5 vol.% O$_2$ in He.

Fig. 8 shows NO conversion to NO$_2$ in 500 ppm NO + 5% O$_2$. LMO-*n* did catalyze NO$_2$ production at low temperature. The activity sequence γ-MnO$_2$ > LMO-7 > LMO-6 > LMO-5 > LMO-4 > LMO was observed, as shown by NO conversion at 200 °C (Table 2). This is in agreement with the fact that Mn-based oxides are effective NO oxidative catalysts [15]. NO$_2$ is not only able to oxidize soot at temperatures as low as room temperature [43], but also converts a solid (soot)-solid (catalyst) reaction to a solid (soot)-gas (NO$_2$) one.

Soot combustion activity was first measured by TPO reactions under loose contact between catalyst and soot in 500 ppm NO + 5 vol.% O$_2$ atmosphere. The carbon mass balance is between 95 and 105%. The

Fig. 13. Soot conversion under the loose contact with catalyst/soot = 10:1 in a gas mixture of 2000 ppm NO + 5 vol.% O_2 in He.

Fig. 12. Soot consumed as a function of time at 120°C over LMO-5 and LMO-6 (a); CO_2 as a function of time concentrations at 120°C over LMO-5 (b) and LMO-6 (c) before and after O_2 is removed from the reactant feed. The curve slopes between two dot lines in (a) represent reaction rates.
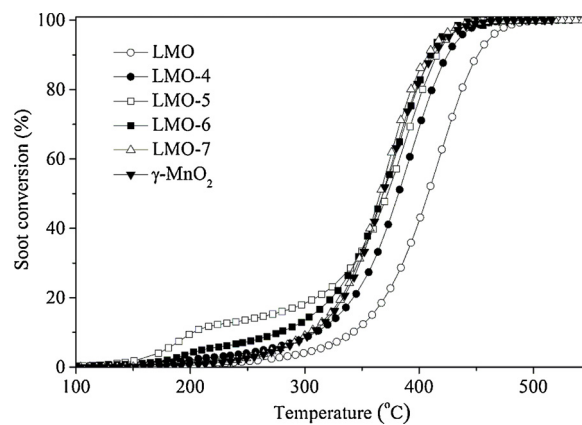
Table 3
Reaction rates, active oxygen density (O*) and TOF values.

Samples	Rate (mol·s^{-1}·g^{-1})×10^{-8}	O* (mol·g^{-1})×10^{-5}	TOF (s^{-1})×10^{-3}
LMO-5	4.50	6.50	0.70
LMO-6	1.48	1.00	1.48

S_{CO_2} is always close to 100% in all cases. As shown in Fig. 9 and Table 2, T_{10} increased in the sequence LMO-6 < LMO-5 < LMO-4 < < LMO-7 ≈ MnO_2 < LMO. Specifically, T_{10} for LMO-6 is 198°C, slightly lower than 200°C, showing significant progress to date [6].

In combination with Fig. S4, the conversion of soot to CO_2 can be resolved into three consecutive steps as the temperature rises (Fig. S4a). As discussed above, the first centred at ~200°C represents soot ignition. The much low T_{10} for LMO-4, LMO-5 and LMO-6 is attributed to the tight contact of soot with ultrathin MnO_{2-x} nanosheets and the improved reducibility as well as NO_2 assistant oxidation as indicated in

Ref. [44,45]. From Fig. S4b-g, NO_x adsorption/desorption on LMO-n is much higher than that on MnO_2, suggesting the stronger oxidation ability for the etching samples, in accordance with H_2-TPR results. This is also confirmed by *in situ* IR of NO adsorption on LMO-6 (as an example) and MnO_2 (Fig. S5). However, NO_2 evolves at lower temperature for MnO_2 (Fig. S4e), which is identical to NO-to-NO_2 stable activity (Fig. 8). It is hypothesized that the strong adsorption of NO_x on LMO-n occupies the active sites for NO oxidation, and thus a slight lower NO-to-NO_2 stable activity is observed for LMO-n than that for MnO_2 (Fig. 8). The second step begins at about 275°C (Fig. S4a) corresponding to the maximum of NO_2 production (Fig. 8). With the consumption of soot, the contact becomes looser than at the ignition step. In this case, the contribution from NO_2 assistant oxidation increases, and thus a slight lower T_{50} is observed for MnO_2 compared with LMO-n. The last step above ~450°C (Fig. S4a) takes a minor fraction of the total combustion. When NO_2 yield reaches the thermodynamic equilibrium, the oxidation with O_2 is dominating.

The slip of NO and NO_2 is detected during soot combustion (Fig. S4b–g), mainly due to the NO-to-NO_2 recycle reactions in which the reduced NO arisen from the NO_2-soot reaction can be re-oxidized again to NO_2 [46]. In addition, low concentrations of N_2O are detected for both LMO-n (Fig. S4d and e for instance) and MnO_2 (Fig. S4g) during TPO. The dependence of the production of CO_2 and N_2O confirms the participation and the incomplete reduction of NO_x. Furthermore, the observation of the N_2O at the ignition step for LMO-n demonstrates the important role of adsorbed NO species for soot ignition [45]. However, MnO_2 is not the case. On the other hand, the presence of NO_x suggests that the simultaneous conversion of soot and NO_x into CO_2 and N_2 is highly desirable [1]. As the most ambitious strategy in this field, the state of the art solution is installed a downstream SCR catalyst (for instance, V_2O_5-WO_3/TiO_2 [47] or Cu-SSZ-13 [48]) to convert all NO_x into N_2. Furthermore, the presence of NO_2 would promote NO_x conversion at lower temperature by a so-called fast SCR (NO + NO_2 + $2NH_3$ = $2N_2$ + $3H_2O$) [49].

Considering the much higher T_{10} for bulk γ-MnO_2 (aggregates, Fig. S1), the observation is initially attributed to the presence of ultrathin MnO_{2-x} nanosheet arrays. For solid nanoparticles, the catalytic reaction occurs only at the outer surface, while for nanosheets the reaction occurs by involving the atoms from both sides leading to much larger active surface areas [50]. As indicated above, on a 1 μm^2 flat surface substrate, the exposed area of the two-sided nanosheets is 250 ×2 × 0.1 μm ×0.1 μm = 5 μm^2, suggesting that the dispersion of soot on these nanosheets is 5 times higher than that on 1 μm^2 substrate. Because soot combustion is a typical solid (catalyst) and solid (soot) reaction systems, the increase in dispersion of soot on the catalyst would greatly improve activity [51,52]. However, this is only one factor. As shown in Fig. 10, the T_{10} values for all samples increase significantly in

5 vol.% O_2 under the same loose contact condition (Table 2), suggesting that a second factor, namely NO_2 content in the atmosphere might play an important role in soot ignition as in CRT [53]. It is well-known that NO_2 is a stronger oxidant than O_2, thus the greater the generation of NO_2, the greater is the activity of soot combustion [54]. As discussed in Fig. 8, the NO-to-NO_2 activity sequence MnO_2 > LMO-7 > LMO-6 > LMO-5 > LMO-4 > LMO, as shown by conversions at 200°C (Table 2), is different from that of T_{10} (Fig. 9 and Table 2), suggesting that the so-called, NO_2 mechanism, cannot alone be responsible for the ignition temperature as low as 198°C under loose contact conditions.

It is necessary to return to the intrinsic activity of catalysts. On one hand, soot combustion is performed in 5 vol.% O_2 under tight contact conditions. As shown in Fig. 11, LMO-5 and LMO-6 show T_{10} of 188 and 192°C, respectively, which are slightly lower than that under 500 ppm NO + 5 vol.% O_2 (Fig. 9 and Table 2), highlighting the importance of the tight contact. Generally, in the absence of NO, the intrinsic activity is represented by H_2-TPR. However, as shown by the initial H_2 consumption rates, the reducibility is not as closely related with the activity as indicated by T_{10} in Fig. 11, suggesting the important role of morphology. For instance, LMO-7 with higher reducibility shows much higher T_{10} when compared with LMO-5, LMO-6 and LMO-4 due to the adhesive nanosheet morphology (Fig. 2j). This also suggests that even though mechanical grinding (milling) is a well-accepted method of producing tight contact between catalyst and soot as employed routinely [55,56] nanosheet catalysts still performed better than nanoparticle counterparts. In the present study, prolonging etching time causes aggregation of nanosheets, which is readily understood from the perspective of decreasing surface energy.

On the other hand, TOFs at 120 °C are measured for LMO-5 and LMO-6 using similar conditions as used in Fig. 11 (Fig. 12). Unfortunately, the accurate values for LMO-4 and LMO-7 cannot be obtained at the same measurement temperature. As listed in Table 3, the reaction rate of LMO-5 is more than 3 times that of LMO-6, confirming the lower T_{10} as shown in Fig. 11. However, the amount of active oxygen (O*) for LMO-5 is more than 6 times that of LMO-6. Consistent with this finding, the higher amount of active oxygen for LMO-5 as LMO-6 is also demonstrated by the O_{ads}/O_{latt} ratio from XPS. TOF values for LMO-5 and LMO-6 are 0.70×10^{-3} and 1.48×10^{-3} s^{-1}, respectively. Although this agrees with the reducibility as reflected by H_2-TPR, the lower T_{10} for LMO-5 than LMO-6 as shown in Fig. 11 confirms the significance of the external factors, namely, the dispersion of soot on the catalysts and NO_2 effects, as discussed above. However, the individual contributions of these factors are difficult to calculate at present because they are normally interrelated.

In order to compare data with previous literature [6], the same experimental conditions were adopted here, namely loose contact condition with catalyst/soot = 10:1 in a gas mixture of 2000 ppm NO + 5 vol% O_2. As shown in Fig. 13 and Table 2, T_{10} = 202°C is observed for LMO-5, which is lower than the 214°C reported on Au@Pt core-shell nanoparticles supported on 3DOM Ce-Zr oxides [6], and thus sets the lowest record to our knowledge for soot combustion.

4. Conclusions

A lowest value yet recorded of T_{10}, ~200 °C was obtained using ultrathin MnO_{2-x} nanosheet array derived from *in situ* etching La layer from $LaMnO_3$. This remarkable soot oxidation performance results from the following three factors: (i) the reducibility is improved significantly by formation of low-coordination ultrathin nanosheet, (ii) the nanosheets promote tight contact of soot with catalyst. Quantitative analysis shows that the dispersion of soot on these nanosheets is 4 times higher than that on the flat substrate, (iii) more NO_2 is formed to ignite soot at a lower temperature in comparison with O_2, and thus further promotes contact between catalyst and soot. This work not only provides a new type of cost-effective noble-metal free catalysts that can activate soot oxidation under cool exhaust conditions, but also present creative soot-oxidation nanocatalyst design and processing strategy for promoting redox property, NO-NO_2 conversion, and tight soot-catalyst contact for catalytic solid (reactant)-solid (catalyst)-gas (oxidant) oxidation reactions at low temperature.

References

[1] D. Fino, S. Bensaid, M. Piumetti, N. Russo, Appl. Catal. A Gen. 509 (2016) 75–96.
[2] A. Bueno-López, Appl. Catal. B: Environ. 146 (2014) 1–11.
[3] F. Gao, J. Szanyi, Appl. Catal. A Gen. 560 (2018) 185–194.
[4] C.A. Neyertz, E.D. Banús, E.E. Miró, C.A. Querini, Chem. Eng. J. 248 (2014) 394–405.
[5] R. Matarrese, S. Morandi, L. Castoldi, P. Villa, L. Lietti, Appl. Catal. B: Environ. 201 (2017) 318–330.
[6] Y. Wei, Z. Zhao, J. Liu, S. Liu, C. Xu, A. Duan, G. Jiang, J. Catal. 317 (2014) 62–74.
[7] N. Guillén-Hurtado, A. García-García, A. Bueno-López, Appl. Catal. B: Environ. 174-175 (2015) 60–66.
[8] C. Davies, K. Thompson, A. Cooper, S. Golunski, S.H. Taylor, M.B. Macias, O. Doustdar, A. Tsolakis, Appl. Catal. B: Environ. 239 (2018) 10–15.
[9] A. Setiabudi, M. Makkee, J.A. Moulijn, Appl. Catal. B: Environ. 50 (2004) 185–194.
[10] G. Cavataio, H.-W. Jen, J.W. Girard, D. Dobson, J.R. Warner, C.K. Lambert, SAE Int. J. Fuels Lubr. 2 (2009) 204–216.
[11] S.J. Schmieg, S.H. Oh, C.H. Kim, D.B. Brown, J.H. Lee, C.H.F. Peden, D.H. Kim, Catal. Today 184 (2012) 252–261.
[12] S. Wagloehner, M. Nitzer-Noski, S. Kureti, Chem. Eng. J. 259 (2015) 492–504.
[13] Z. Hong, Z. Wang, X. Li, Catal. Sci. Technol. 7 (2017) 3440–3452.
[14] C.H. Kim, G. Qi, K. Dahlberg, W. Li, Science 327 (2010) 1624–1627.
[15] W. Wang, G. McCool, N. Kapur, G. Yuan, B. Shan, M. Nguyen, U.M. Graham, B.H. Davis, G. Jacobs, K. Cho, X. Hao, Science 337 (2012) 832–835.
[16] N. Tang, Y. Liu, H. Wang, Z. Wu, J. Phys. Chem. C. 115 (2011) 8214–8220.
[17] C. Cao, Y. Zhang, D. Liu, M. Meng, Small 11 (2015) 3659–3664.
[18] A. Ma, L. Gu, Y. Zhu, M. Meng, J. Gui, Y. Yu, B. Zhang, Chem. Commun. 53 (2017) 8517–8520.
[19] C. Cao, X. Li, Y. Zha, J. Zhang, T. Hu, M. Meng, Nanoscale 8 (2016) 5857–5864.
[20] D. Jampaiah, V.K. Velisoju, P. Venkataswamy, V.E. Coyle, A. Nafady, B.M. Reddy, S.K. Bhargava, ACS Appl. Mater. Interfaces 9 (2017) 32652–32666.
[21] F. Fang, N. Feng, L. Wang, J. Meng, G. Liu, P. Zhao, P. Gao, J. Ding, H. Wan, G. Guan, Appl. Catal. B: Environ. 236 (2018) 184–194.
[22] N.D. Wasalathanthri, T.M. SantaMaria, D.A. Kriz, S.L. Dissanayake, C.H. Kuo, S. Biswas, S.L. Suib, Appl. Catal. B: Environ. 201 (2017) 543–551.
[23] Y. Cheng, W. Song, J. Liu, H. Zheng, Z. Zhao, C. Xu, Y. Wei, E.J.M. Hensen, ACS Catal. 7 (2017) 3883–3892.
[24] V. Alcalde-Santiago, A. Davó-Quiñonero, D. Lozano-Castelló, A. Bueno-López, Appl. Catal. B: Environ. 234 (2018) 187–197.
[25] H. Xu, N. Yan, Z. Qu, W. Liu, J. Mei, W. Huang, S. Zhao, Environ. Sci. Technol. 51 (2017) 8879–8892.
[26] S.Y. Chen, W. Song, H.J. Lin, S. Wang, S. Biswas, M. Mollahosseini, C.H. Kuo, P.X. Gao, S.L. Suib, ACS Appl. Mater. Interfaces 8 (2016) 7834–7842.
[27] B. Bai, J. Li, J. Hao, Appl. Catal. B: Environ. 164 (2015) 241–250.
[28] H. Jiang, Q. Wang, H. Wang, Y. Chen, M. Zhang, ACS Appl. Mater. Interfaces 8 (2016) 26817–26826.
[29] Y. Peng, W. Si, J. Li, J. Crittenden, J. Hao, Catal. Sci. Technol. 5 (2015) 2478–2485.
[30] W. Si, Y. Wang, Y. Peng, J. Li, Angew. Chem. Int. Ed. 54 (2015) 7954–7957.
[31] W. Si, Y. Wang, S. Zhao, F. Hu, J. Li, Environ. Sci. Technol. 50 (2016) 4572–4578.
[32] M.H. Alfaruqi, V. Mathew, J. Gim, S. Kim, J. Song, J.P. Baboo, S.H. Choi, J. Kim, Chem. Mater. 27 (2015) 3609–3620.
[33] M. Piumetti, B. van der Linden, M. Makkee, P. Miceli, D. Fino, N. Russo, S. Bensaid, Appl. Catal. B: Environ. 199 (2016) 96–107.
[34] A. Carrascull, C. Grzona, D. Licka, M. Ponzi, E. Ponzia, React. Kinet. Catal. Lett. 75 (2002) 63–68.
[35] Z. Zhang, D. Han, S. Wei, Y. Zhang, J. Catal. 276 (2010) 16–23.
[36] Y. Sun, S. Gao, F. Lei, Y. Xie, Chem. Soc. Rev. 44 (2015) 623–636.
[37] C. Lee, Y. Jeon, S. Hata, J. Park, R. Akiyoshi, H. Saito, Y. Teraoka, Y.G. Shul, H. Einaga, Appl. Catal. B: Environ. 191 (2016) 157–164.
[38] X. Wang, Y. Zhang, Q. Li, Z. Wang, Z. Zhang, Catal. Sci. Technol. 2 (2012) 1822–1824.
[39] Y.N. Lee, R.M. Lago, J.L.G. Fierro, V. Cortés, F. Sapiña, E. Martínez, Appl. Catal. A Gen. 207 (2001) 17–24.
[40] S. Ponce, M.A. Peña, J.L.G. Fierro, Appl. Catal. B: Environ. 24 (2000) 193–205.
[41] X. Tang, J. Li, L. Sun, J. Hao, Appl. Catal. B: Environ. 99 (2010) 156–162.
[42] Y. Liu, H. Dai, Y. Du, J. Deng, L. Zhang, Z. Zhao, Appl. Catal. B: Environ. 119-120 (2012) 20–31.
[43] J. Zawadzki, M. Wiśniewski, K. Skowrońska, Carbon 41 (2003) 235–246.
[44] K. Tikhomirov, O. Kröcher, M. Elsener, A. Wokaun, Appl. Catal. B: Environ. 64

(2006) 72–78.

[45] H. Zhang, C. Zhou, M.E. Galvez, P.D. Costa, Y. Chen, Appl. Surf. Sci. 462 (2018) 678–684.

[46] Z. Feng, Q. Liu, Y. Chen, P. Zhao, Q. Peng, K. Cao, R. Chen, M. Shen, Shan B, Catal. Sci. Technol. 7 (2017) 838–847.

[47] M. Zhu, J.K. Lai, U. Tumuluri, Z. Wu, I.E. Wachs, J. Am. Chem. Soc. 139 (2017) 15624–15627.

[48] U. Deka, I. Lezcano-Gonzalez, B.M. Weckhuysen, A.M. Beale, ACS Catal. 3 (2013) 413–427.

[49] C. Paolucci, I. Khurana, A.A. Parekh, S. Li, A.J. Shih, H. Li, J.R. Di Iorio, J.D. Albarracin-Caballero, A. Yezerets, J.T. Miller, W.N. Delgass, F.H. Ribeiro, W.F. Schneider, R. Gounder, Science 357 (2017) 898–903.

[50] R. Mas-Balleste, C. Gomez-Navarro, J. Gomez-Herrero, F. Zamora, Nanoscale 3 (2011) 20–30.

[51] H. Zhao, X. Zhou, W. Huang, L. Pan, M. Wang, Q. Li, J. Shi, H. Chen, ChemCatChem 10 (2018) 1455–1463.

[52] Q. Yang, F. Gu, Y. Tang, H. Zhang, Q. Liu, Z. Zhong, F. Su, RSC Adv. 5 (2015) 26815–26822.

[53] J. Oi-Uchisawa, S. Wang, T. Nanba, A. Ohi, A. Obuchi, Appl. Catal. B: Environ. 44 (2003) 207–215.

[54] W. Kaspera, P. Indyka, Z. Sojka, A. Kotarba, Catal. Sci. Technol. 8 (2018) 3183–3192.

[55] J.P.A. Neeft, M. Makkee, J.A. Moulijn, Appl. Catal. B: Environ. 8 (1996) 57–78.

[56] S. Liu, X. Wu, D. Weng, R. Ran, J. Rare Earths. 33 (2015) 567–590.